Heteroepitaxial recrystallization: A new mechanism discovered in a polycrystalline γ-γ' nickel based superalloy

Marie-Agathe Charpagne, Thomas Billot, Jean-Michel Franchet, Nathalie Bozzolo

Heteroepitaxial recrystallization: a new mechanism discovered in a polycrystalline γ-γ' nickel based superalloy

Marie-Agathe Charpagne [1,2], Thomas Billot [2], Jean-Michel Franchet [3], Nathalie Bozzolo [1]

[1] MINES ParisTech, PSL - Research University, CEMEF - Centre de mise en forme des matériaux, CNRS UMR 7635, CS 10207 rue Claude Daunesse 06904 Sophia Antipolis Cedex, France
[2] Snecma-Safran Group, Technical Department, 171 boulevard de Valmy – BP 31, 92702 Colombes Cedex, France
[3] Safran SA, SafranTech – Materials & Process Department, Magny-Les-Hameaux Cedex, France

Abstract

The dynamic recrystallization mechanisms and kinetics of a recently developed γ-γ' nickel based superalloy are studied at different subsolvus temperatures. Special care is paid to the evolution of γ' particles and their influence on recrystallization phenomena. An original dynamic recrystallization mechanism is highlighted thanks to the combined use of Energy Dispersive Spectrometry and Electron BackScattered Diffraction mapping techniques. This mechanism leads to the formation of large heteroepitaxial pairs, made of a primary precipitate embedded in a recrystallized grain having the same crystallographic orientation. Recrystallization nuclei arise from inverse precipitation of γ phase at the rim of primary γ' precipitates, prior to deformation. This heteroepitaxial recrystallization mechanism is reported here for the first time. It controls dynamic microstructure evolution at low strains and is then progressively replaced by the conventional discontinuous necklace recrystallization process at higher strains.

Keywords: **γ-γ'** nickel based superalloys, inverse precipitation, dynamic recrystallization, heteroepitaxy, γ' precipitates, microstructure.

Introduction

Grain size control is of utmost importance for polycrystalline nickel based superalloys used in high temperature applications like aerojet turbine disks, as the material must resist to both creep and thermomechanical fatigue under severe conditions [1]. Many studies are therefore devoted to recrystallization mechanisms in γ-γ' superalloys [2–8]. Those materials are highly alloyed, and consequently may contain second phase particles and precipitates. As any γ-γ' nickel based superalloy, the recently developed René 65^{TM} alloy mainly consists in a FCC matrix strengthened by a high volume fraction of γ' precipitates [9]. The size distribution of γ' particles evolves during hot-processing. The so-called primary particles are formed during the early stages of the industrial process, while transforming the ingot into a billet. They are generally multi-micrometric and aim at pinning the grain boundaries during further forging steps in the sub-solvus domain. As a consequence, those precipitates are expected to be mostly located on grain boundaries and at triple junctions in the recrystallized microstructures obtained after forging [10]. Secondary and tertiary precipitates are much smaller (typically few hundreds and few tens of nanometers respectively). They are intragranular, form

coherently with their hosting grain and play a key role in the material hardening. Both secondary and tertiary precipitates are partially or fully dissolved at the sub-solvus forging temperatures [11,12] and they form again during cooling. The size distribution and morphology of secondary and tertiary precipitates depend on the cooling rate [13–19]. The fine γ' precipitation state in industrial parts is tuned by specific thermal treatments performed after the whole forging sequence in order to achieve optimal properties. Bond et al. [9] have reported the presence of other types of particles in the René 65^{TM} alloy, mostly titanium nitride TiN (with typical facetted morphology), borides (enriched in Mo, W and Cr, spheroïdal, about 1 µm in diameter) and, more rarely, titanium carbides (enriched in Nb and W).

In addition to the pinning force exerted on grain boundaries [20], large particles (typically 1µm and more) may also induce preferential nucleation sites for recrystallization. If those large second phase particles are harder than the matrix (which is the case for nitrides, borides and primary γ' precipitates), a heterogeneous strain field develops around them during deformation. Due to the locally higher dislocation density and to the resulting orientation gradient, the neighborhood of the hard particle is a preferential nucleation site for recrystallization. Groups of recrystallized grains are then observed close to the second phase particles. This process, called Particle Stimulated Nucleation (PSN) is well documented in the literature [21–30]. It is worth mentioning that recrystallized grains arising from PSN have no particular orientation relationship relative to the involved second phase particle.

The present article demonstrates that primary γ' precipitates can indeed act as nucleation sites for dynamic recrystallization, but by a process which is drastically different from PSN. As shown below, recrystallized grain nuclei arise from γ' to γ phase transformation at the rim of primary γ' precipitates, prior to deformation. This new mechanism is called heteroepitaxial recrystallization because recrystallized grains have the same crystallographic orientation as the precipitate they arise from. Its kinetics, dependency on deformation conditions, as well as its interaction with conventional dynamic recrystallization mechanisms are discussed in detail in the following.

1. Material and experimental setup

René 65^{TM} is a commercial polycrystalline γ-γ' nickel based superalloy, which nominal composition in wt% is 13 Cr- 16 Co- 3.7 Ti- 2.1 Al- 4 Mo- 4 W-1 Fe- 0.7 Nb- 0.05 Zr, 0.016 B, balance Ni [31]. Double-cone shaped samples were withdrawn from an industrially forged piece. Such piece may contain remnant stored energy, which would be inconvenient for the present recrystallization study. In order to start from a controlled metallurgical state, the samples have thus been hold for two hours at 1050°C prior to any further investigation. After annealing samples were cooled at 5°C per minute down to 600°C and then air-cooled down to room temperature. The aim of the plateau was to dissolve secondary and tertiary precipitates and allow recovery to occur while keeping primary γ' precipitates so as to maintain the grain size close to the one of as-received state. The slow-cooling step was applied to form again secondary γ' precipitates, but in a controlled manner, so that their effect on the

recrystallization behavior of the alloy could also be assessed. The annealed samples were then deformed using a MTS 250 compression-testing machine equipped with a tubular furnace (MTS 653). The range of applied conditions covers temperatures between 1000°C and 1070°C, nominal strain rates of 0.01 and 0.1 s^{-1}, and deformation levels up to 1.5. The double-cones sample geometry induces a well-controlled strain (and strain rate) gradient along the radius, from zero at the rim to a maximal value at the center that depends on the geometry. Two geometries were actually used (Fig. 1): A-type samples with a maximum strain of 1.4 and B-type samples with a maximal strain of 0.36. The samples were introduced in the hot furnace with a thermocouple welded on their surface, and were deformed as soon as they reached the target temperature. The time for reaching the deformation temperature was in any case less than 10 minutes. After deformation, samples were water-quenched within three seconds, in order to limit post-dynamic evolutions as much as possible. Deformed samples were cut and polished in the in-diameter cross-section in order to characterize microstructure along the mid-thickness radius (dashed line on Fig. 1). A surface quality suitable for Electron Back-Scattered Diffraction (EBSD) was achieved by mirror polishing using diamond suspensions down to 1 µm followed by vibratory polishing with colloidal silica. Microstructures were characterized using a Zeiss Supra40 Field Emission Gun – Scanning Electron Microscope (FEG-SEM) operating at 15kV and equipped with a Bruker Esprit® package including Energy Dispersive Spectrometry (EDS) and EBSD. The coupled EDS-EBSD mapping technique was employed as described in [32] and allowed to discriminate primary γ' precipitates from small γ grains. BackScattered Electron (BSE) images were used to provide a better-resolved description of the morphology and location of γ' precipitates. A thin foil was also prepared for performing complementary Transmission Electron Microscopy (TEM) analyses. The thin foil is a cross-section of a primary γ' precipitate and was prepared by Focused Ion Beam (FIB) micromachining in a FEI dual-beam FIB/SEM equipped with a Gallium source. Chemical analyses were performed on that thin foil by EDX in a FEI Titan TEM operated at 200 kV.

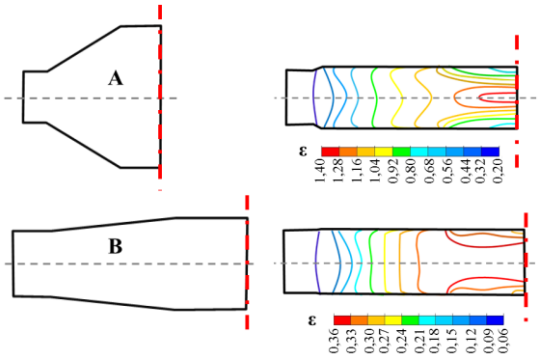

Figure 1: Schematic views of the two double-cone sample geometries (A-type and B-type), before (left) and after deformation (right). The iso-strain levels plotted on the deformed sample schemes have been obtained by numerical simulation of the compression test using the Forge® software.

The EDAX-TSL OIM® software was used for EBSD data post-processing. The threshold misorientation angle applied to define a grain boundary was settled to 15°. Twin boundaries (60°<111> with a tolerance of 5°) were not considered as grain boundaries but as internal crystal defects. Recrystallized grains have been identified thanks to their relatively low

dislocation density, and thus relatively low internal misorientation level, compared to the initial matrix grains. They could be separated based on the Grain Orientation Spread (GOS) value, which is the average misorientation angle between each pixel of a grain and the average orientation of all the pixels of the grain.

The γ' precipitate distribution was obtained by filtering BSE images using the Noesis Visilog® software. Fig. 2 shows a typical example of a BSE image exhibiting a suitable phase contrast, its filtered version highlighting the detected particles with a random color, and the corresponding particle size distribution. About 4500 particles were counted for each analyzed sample. A special care was given to the accurate quantification of small γ' precipitates, as shown in the inserts of Figs. 2-a and b.

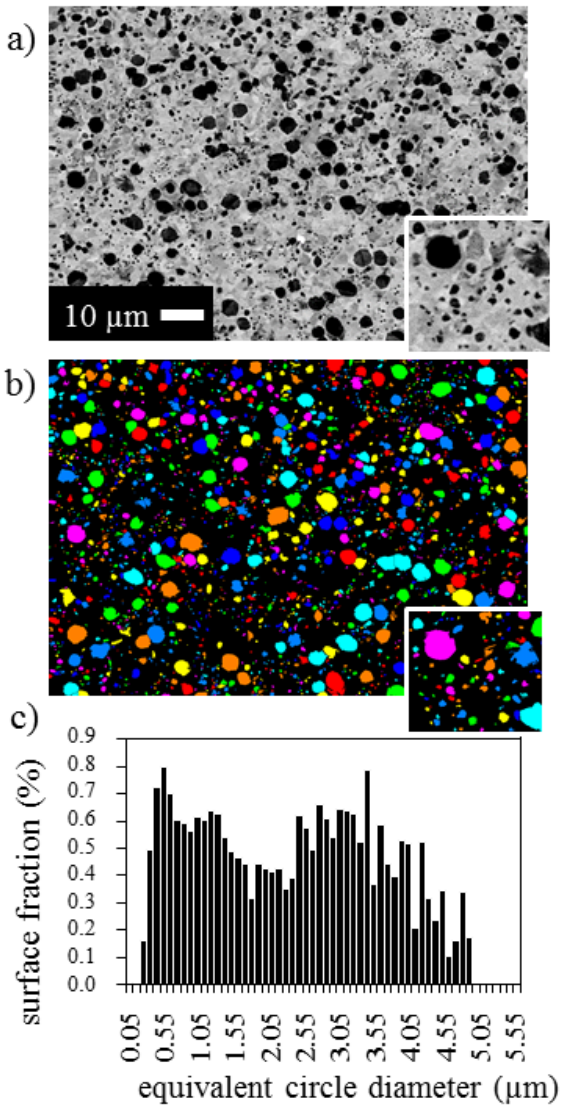

Figure 2: Precipitation state after deformation at 1000°C and 0.01s^{-1} to ε=0.6. a) BSE image exhibiting phase contrast, b) filtered image (Visilog), c) corresponding particle size distribution.

2. Results and discussion

2.1. Effect of the preliminary annealing

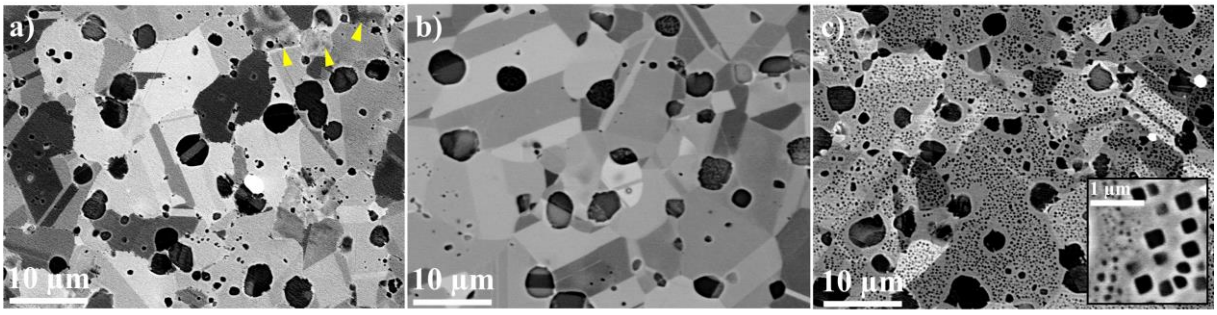

Figure 3: BSE images of the microstructure evolution during the recovery annealing performed on the as-received state. a) as-received state, b) after 2 hours at 1050°C followed by water quenching, c) after 2 hours at 1050°C and slow cooling down to 600°C at 5°C/min and then air cooling down to room temperature.

The as-received material (Fig. 3-a) is an air-cooled industrially forged piece. Its microstructure consists in fine grains (10 µm in average) pinned by primary γ' particles. The latter have a spheroidal shape and are all located on grain boundaries or at triple junctions. Few grains (arrowed on Fig. 3-a) exhibit non-uniform BSE intensity, which indicates the presence of orientation gradients and thus of dislocations. In other words, the as-received microstructure is not fully recrystallized. In addition, the intragranular fine γ' precipitation is rather inhomogeneous. Fig. 3-b shows the microstructure after two hours holding at 1050°C and water-quenching. The original 10 µm average grain size is kept, thanks to the primary γ' precipitates which were maintained. Most intragranular precipitates were dissolved. The grains exhibit homogeneous BSE intensity, which indicates that they don't have internal misorientation anylonger and that recovery or recrystallization occurred. EBSD has been performed on microstructure of Fig. 3-b ; the average GOS value is indeed below the measurement accuracy of the EBSD technique (about 0.5° under the actual acquisition setup). The preliminary annealing was thus successful for homogenizing and resetting the stored energy to a very low level in the microstructure. The effect of the slow-cooling is shown on Fig. 3-c: two populations of intragranular precipitates have formed. The larger ones are cuboidal secondary precipitates with an average size of 0.45 µm; tertiary ones are spheroidal and much smaller, with an average diameter of less than 50 nm (see the insert in Fig. 3-c). The metallurgical state of Fig. 3c has been used as starting state for all the experiments detailed below.

2.2. Microstructure evolution during deformation at 1000°C and $0.1s^{-1}$

A typical microstructure evolution sequence observed in the sample deformed at 1000°C and $0.1s^{-1}$ is presented on Fig. 4, with increasing strain from left to right. The color code is based on the GOS parameter, which can be semi-quantitatively interpreted as representative for the dislocation density or the stored energy. The newly recrystallized grains appear in blue and deformed ones in green to red. EDS-resolved γ' precipitates appear black. From a global point of view, with increasing strain, the initial microstructure is progressively invaded by finer

recrystallized grains. At very low strains (ε=0.5, Fig. 4-a) the γ grain structure is still very close to the initial one, equiaxed with an average grain size of 10 µm. At the maximum applied strain level (ε=1.40, Fig. 4-e), the γ grain size is much smaller, about 1 µm. Two domains can actually be identified on Fig. 4 when considering the location of the recrystallized grains. The first domain covers low strain levels (0 to 0.60) and is characterized by recrystallized grains embedding primary γ' precipitates (detailed in section 2.2.1); the second domain starts at a strain of 0.60 and extends towards the maximum strain and is characterized by recrystallized grains appearing at the former matrix grain boundaries (detailed in section 2.2.2).

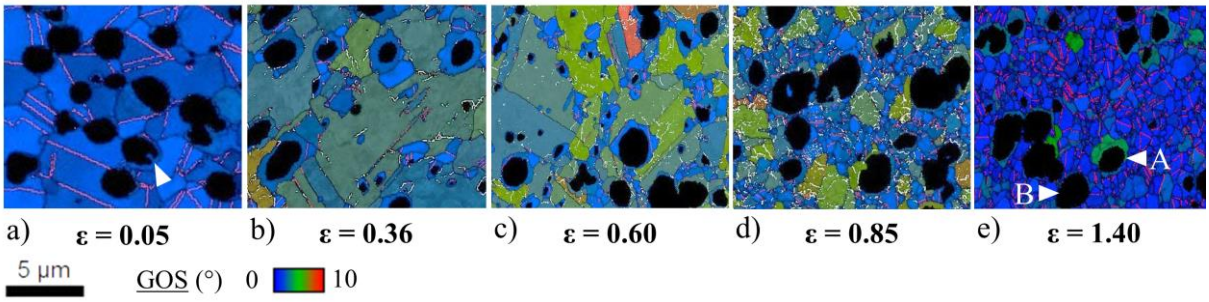

Figure 4: Microstructure evolution at 1000°C and 0.1s^{-1}, with increasing strain level from a) to e). EBSD maps plotted with a GOS-based color code. Primary γ' precipitates appear in black. Grain boundaries (misorientations >15°) are plotted in black, sub-boundaries (2° to 15°) in light grey and twin boundaries (60° <111> with a tolerance of 5°) in red.

2.2.1. Heteroepitaxial recrystallization in the low strain domain (0 – 0.60)

In the low strain domain, a first population of recrystallized grains develops. They are unusually located around primary γ' precipitates, each primary γ' precipitate being associated with only one recrystallized grain and being embedded inside its recrystallized grain. At the lowest strain level (ε=0.05, Fig. 4-a), the energy stored in the matrix is still not detectable by the GOS method, the average GOS value being in the range of the angular resolution of the EBSD technique (0.5°). The grain boundaries of the matrix grains are smooth and annealing twin boundaries are preserved. With increasing strain to ε=0.36 (Fig. 4-b), each primary γ' becomes fully surrounded by a unique recrystallized grain. Once all primary γ' precipitates are in this configuration, no appearance of such recrystallized grain can occur anymore; the already formed grains just grow up. Fig. 5 shows a wider area of the EBSD map taken at the intermediate strain of 0.36, with different color codes : GOS map (Fig. 5-a), EDX-resolved phase map (Fig. 5-b) and orientation map (Fig. 5-c). The phase map shows that all primary γ' precipitates are embedded in a recrystallized γ grain; none of them is located on the matrix grain boundaries anymore. Fig. 5-c reveals another striking characteristic of those recrystallized grains: they have the same orientation as the embedded precipitate. The disorientation profile shown on Fig. 5-d shows a slight orientation gradient (about 0.5°.µm^{-1}) in the precipitate and almost no orientation gradient in the freshly recrystallized surrounding grain, but no significant misorientation associated with the interphase boundary. If any, the misorientation between both phases is below the EBSD angular resolution. The existence of such coherent recrystallized grains, including a finer characterization of the coherent γ-γ' interphase boundary, has been recently reported by the authors in [32]. In the following, this

specific population of recrystallized grains will be denoted heteroepitaxially recrystallized (HERX) grains.

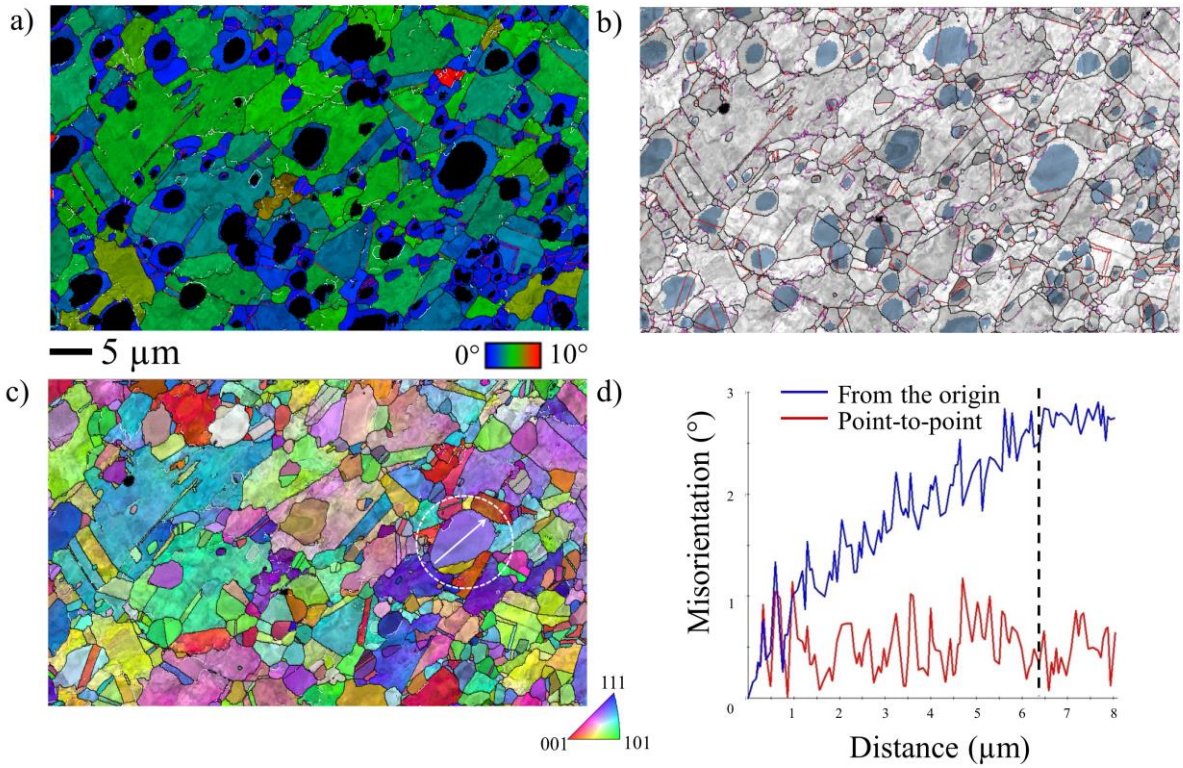

Figure 5: Microstructure after deformation at T=1000°C and 0.1s^{-1} to ε=0.36. a) GOS map, b) EDS resolved phase map (γ' phase in light blue), c) Orientation map within a color code indicating which crystallographic direction is parallel to the normal to the scanned section, d) Misorientation profile across a γ' precipitate and its HERX grain (white arrow on c)). The interphase boundary position is indicated by a dashed line. All maps are superimposed with the Index of Quality map, grain boundaries (misorientation angles >10°) are represented in black and annealing twins in red.

A closer look back into the microstructure of Fig. 4-a reveals that HERX grains already started to form after only 0.05 strain. Primary γ' precipitates exhibit a thin γ shell, which can hardly be spatially-resolved using the coupled EDS-EBSD technique, but are nevertheless visible around some precipitates, as the ones arrowed on Fig. 4-a. This is confirmed by the BSE images of Fig. 6.

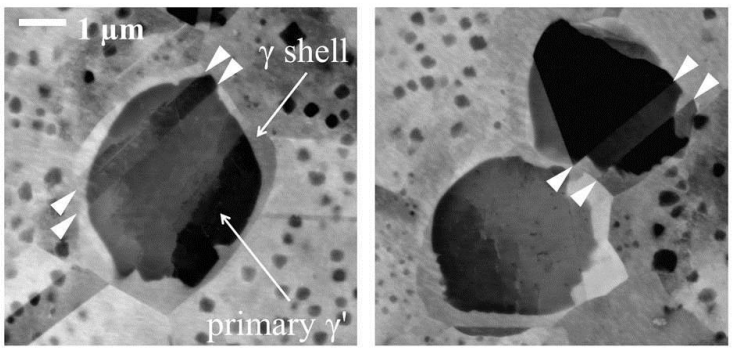

Figure 6: Sample deformed at 1000°C, 0.1s^{-1} and ε=0.05. BSE images showing primary γ' precipitates with a thin γ shell. Annealing twin crossing both the precipitate and the γ shell are arrowed.

2.2.2. Discontinuous necklace recrystallization at higher strains (>0.60)

Above the strain of 0.60, another population of recrystallized grains nucleates at the boundaries of the matrix grains. With increasing strain, the intragranular misorientations have significantly increased in the matrix as a result of dislocation storage. In addition, the matrix grain boundaries have become serrated as a result of heterogeneities in the stored energy field, providing preferential nucleation sites for the new population of recrystallized grains. The resulting necklace-like topology is visible on the GOS map presented on Fig. 4-c. As the strain increases, those grains progressively invade the deformed matrix, by simultaneous nucleation and growth phenomena. This mechanism is very common and well documented in the literature as discontinuous dynamic recrystallization (DDRX in the following). At the maximum strain of 1.4, the remaining matrix has been completely consumed and replaced by DDRX grains. Simultaneously, the dislocation density in the HERX grains increased. As they formed early in the deformation process, they got progressively deformed and have stored dislocations with increasing strain, as visible on the GOS map Fig. 4-e. The average GOS value of the HERX grains reaches 2.0°, against only 0.7° for the DDRX grains which appeared later. Some HERX grains are still visible around primary γ' precipitates; a typical example is labelled A on Fig. 4-e. Other HERX grains have completely or partially disappeared (example labelled B). Some of the HERX grains had thus stored enough energy that they could be consumed by the growing DDRX grains (having a lower stored energy level).

To summarize, there are clearly two distinct recrystallization mechanisms leading to very different populations of recrystallized grains. They differ by their location, morphology and size, and by the strain range at which they develop. Given that, both populations may evolve differently with varying deformation conditions, as investigated in the following section.

2.3 Influence of temperature on recrystallization mechanisms and kinetics, at a strain rate of $0.01s^{-1}$

To separate the recrystallized populations identified here above a double threshold was applied on the EBSD maps. The first threshold is based on the GOS parameter and enables to isolate all recrystallized grains from the deformed ones. A second threshold was applied to distinguish HERX and DDRX recrystallized grains, either based on the grain size or on the GOS parameter again. In some cases, the recrystallized populations were separated manually, based on their morphology. For all deformation conditions, the recrystallized populations could thus be analyzed separately in terms of area fraction, grain size and average intragranular misorientation.

Figure 7 presents the kinetics of both HERX and DDRX at 1000°C, 1040°C and 1070°C, for the same nominal strain rate of $0.01s^{-1}$. Similar influence of temperature on microstructure evolution has been observed in the experiments performed at a nominal strain rate of 0.1 s^{-1}, but less pronounced. It is worth mentioning here that the influence of the strain rate cannot be

more accurately analyzed from such double-cone compression experiments, since the actual strain rate varies along the radius.

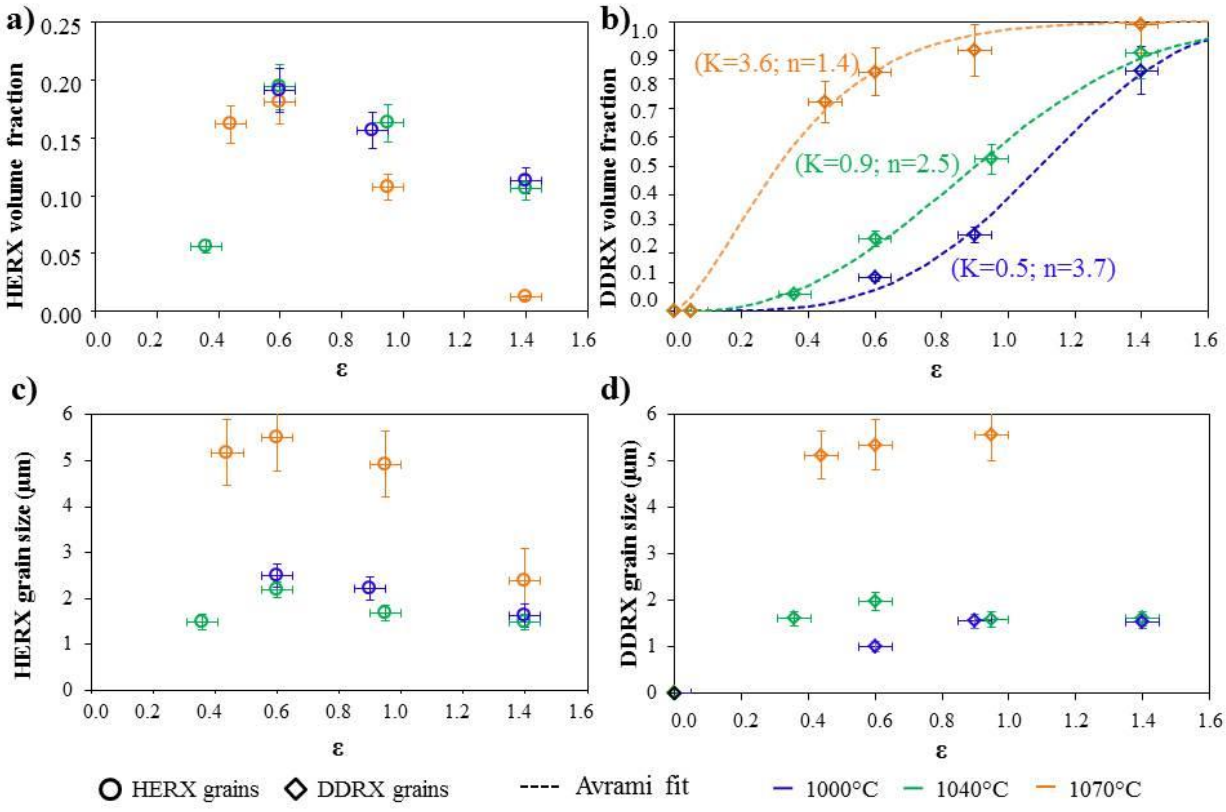

Figure 7: Kinetics of both HERX and DDRX recrystallization mechanisms at 0.01s^{-1} and temperatures of 1000°C, 1040°C and 1070°C. a) HERX volume fraction, b) DDRX volume fraction, c) HERX grain size, d) DDRX grain size.

HERX grains always appear and grow first (i.e. at low strain levels), reaching maximum volume fraction and size around ε=0.60 for all temperatures. The DDRX grains then appear with a delay. They continuously nucleate and grow so that their average size is almost constant. The development of the DDRX population is correlated with the shrinkage of the HERX one. The DDRX mechanism obviously becomes predominant at high strain levels. The DDRX kinetics is faster as temperature increases, and so is the shrinkage of the HERX grains. From Fig. 7-a, the maximum HERX fraction is similar at all three temperatures. However, although the results obtained at 1000°C and 1040°C are very close to each other, a gap is observed in between those two and the highest temperature. The most striking difference concerns the maximum HERX grain size (calculated as the diameter of the disk having the same surface area as the HERX ring-shaped grain), which is 5.5 µm at 1070°C, twice larger than those reached at 1000°C and 1040°C (2.2 µm and 2.5 µm, respectively). Fig. 7-d shows that the DDRX grain size rapidely reaches a steady-state value. For all temperatures, the evolution of the DDRX fraction could be well fitted with a sigmoidal Avrami-type law:

$$f_{DDRX} = 1 - \exp(-K\varepsilon^n) \quad (5)$$

The K and n coefficients have been determined by using the least squares method. From the obtained results, the evolution of both K and n is monotonous: K decreases and n increases

with increasing temperature. The obtained values of n are in the same range than those obtained on Waspaloy in the sub-solvus domain by Semiatin et al. [30]. The coefficients also suggest a decreasing incubation time and an accelerated growth regime with increasing temperature.

Although a fully recrystallized microstructure could not be achieved at 1000°C, the steady-state DDRX grain sizes at 1000°C and 1040°C are very close (1.5 µm and 1.6 µm in average, respectively). Here again, the average grain size reached at 1070°C is much higher than those at the two lower temperatures.

2.4. On the nucleation of HERX grains

As presented in sections 2.2 and 2.3, the growth of HERX grains starts right from the early stages of deformation, even at the lowest tested temperature 1000°C. This suggests either a very fast nucleation mechanism (quite unlikely since classical nucleation requires a minimal stored energy level), or a nucleation phenomenon that already occurred before deformation.

Primary precipitates after the preliminary annealing with slow cooling are shown on Figs. 8-b to 8-d. Their shape is very irregular as compared to the rounded one obtained after the same annealing but ended with water-quenching (Fig. 8-a). The BSE image of Fig. 8-b suggests that small volumes of a new phase with a similar intensity as the γ matrix has formed at the rim of the precipitate. Annealing twin boundaries (arrowed on Fig. 8-b) crossing the whole domain is a strong clue for supporting the idea that those brighter areas are coherent γ pieces. Moreover, this morphology is very close to the one observed in the 0.05 strained sample of Fig. 6. Those bright features are very likely to be the nuclei which will lead to the HERX grains. No such feature has been observed after holding at 1050°C and quenching, which means that they formed during slow cooling.

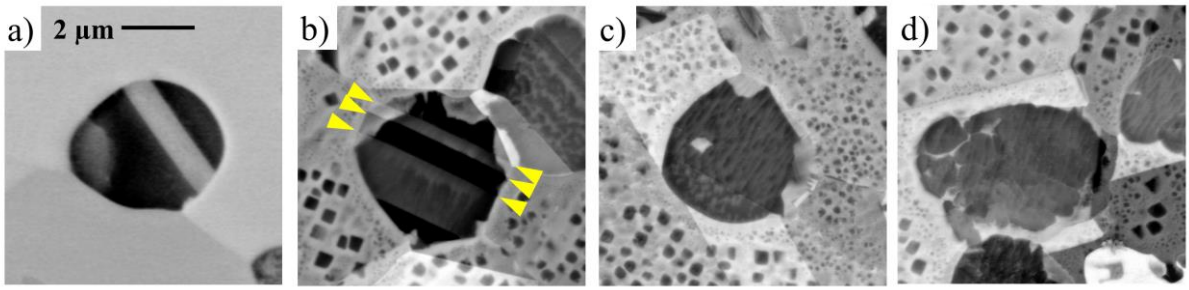

Figure 8: Primary γ' precipitates after a) two-hours annealing at 1050°C and quenching, b-c-d) two-hours annealing at 1050°C and slow cooling at 5°C/min, down to 600°C: b) annealing twins crossing the whole precipitate, c) presence of an inner γ particle, d) split precipitate.

In order to confirm the nature of the γ phase forming at the rim of primary γ' precipitates during slow cooling, a cross-section has been prepared for TEM analyses from the sample of Figs. 8-b-c-d. A primary γ' precipitate with bright areas at the rim has been selected (Fig. 9-a) and the cross-section (dashed area) has been cut perpendicular to the image. A STEM bright field image is shown on Fig. 9-b and labeled on the scheme of Fig. 9-c. The chemical composition of the different areas measured by EDX is given in Table 1.

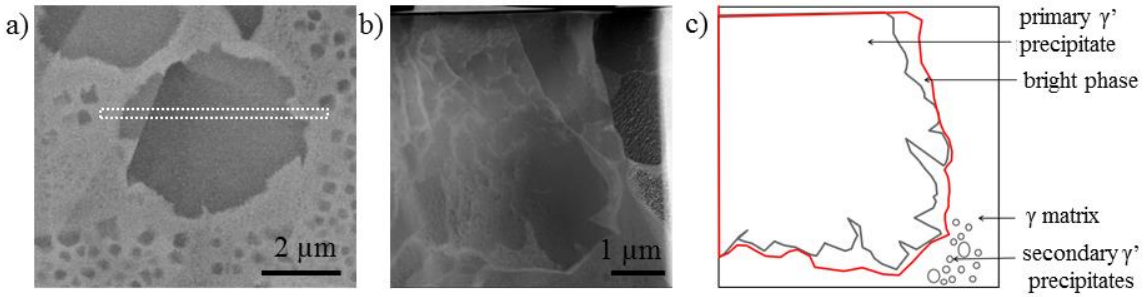

Figure 9: Annealed and slow cooled microstructure. a) BSE image of the selected precipitate, the rectangular area corresponds to the section across which the thin foil has been extracted; b) STEM image of the thin foil; c) scheme of the different features observed in the thin foil with labels.

Element	*Ni*	*Co*	*Cr*	*Al*	*Ti*	*Mo*	*Nb*	*W*	*Fe*
primary γ' precipitate	75.1	7.1	1.5	4.5	10.3	-	0.8	-	0.8
γ matrix	49.6	17.3	22.9	0.3	0.6	4.9	-	3.1	1.2
bright phase at the rim of the precipitate	46.6	16.5	23.3	0.4	0.5	4.2	-	7.1	1.4

Table 1: chemical composition (wt%) of the different features observed in the thin foil, measured by EDX in a TEM.

The bright phase at the rim of the primary precipitate is enriched in Co and Cr, which are typical γ-gene elements, and is depleted in Ti and Al, the γ'-formers. Its composition is very similar to the one of the γ matrix. The only significant difference (within the accuracy of EDS) is a higher W content. From those observations, this bright phase is thus confirmed to be γ phase.

Although the detailed microstructural mechanism by which the nucleation of γ phase at the rim of primary γ' precipitates is out of scope of this article, it appears that a phase transformation occurring in the primary γ' precipitates is at the origin of the formation of HERX nuclei. The formation of γ phase inside γ' particles is a phenomenon known as "inverse precipitation" in the literature. Such a mechanism has never been reported in conditions similar to our experiments. However, it is well documented in nickel based superalloys submitted to ageing treatments, in which the undercooling is greater. Radavich and Couts first observed some tiny particles in the large precipitates of a complex alloy following an elevated temperature exposure [33] and then in overaged Udimet 700 [34] . Deeper characterizations conducted by Merrick [35] on similar particles observed in thermally treated Inconel 738 have enabled to identify those small particles as being γ phase. In more recent studies [36–39], the presence of similar FCC Cr-enriched particles inside primary γ' precipitates has been reported in the N18 nickel-based superalloy [37,39], and in a nickel-cobalt based superalloy [38] when submitted to ageing treatments.

The common feature about all those studies that the materials have undergone two thermal treatments: a first one at high (but still sub-solvus) temperature, and a second one at a much lower temperature (usually an ageing treatment). Although the reported particle morphologies are drastically different from those observed in our samples, the underlying driving force for the γ'→ γ transformation may be the same. Oblak et al. [40] have identified the supersaturation of γ-gene elements in γ' precipitates as being the driving force for the formation of γ particles during ageing treatments. When a γ/γ' superalloy, initially at thermodynamic equilibrium at a temperature T_1, is exposed to a temperature T_2 lower than T_1,

the γ' precipitates become supersaturated in γ-gene elements, which thus have a tendency to be rejected out. If a sufficient amount of γ-gene elements are present in the γ' precipitate, a tiny γ particle can be formed inside the considered precipitate [35–37,40]. In the present study, inverse precipitation occurs during slow cooling after 2h holding at 1050°C, as undercooling increases while decreasing temperature. The evolution of equilibrium composition and volume fraction of both γ and γ' phases with temperature has been calculated for the René 65^{TM} alloy using the Thermo-Calc software (Fig. 10-b-c). While decreasing temperature, the matrix becomes supersaturated in γ'-gene elements (Al, Ti), and the γ' phase becomes supersaturated in γ-gene elements (Cr, Co, Mo). On one hand, the supersaturation of γ'-gene elements leads -very classically- to the formation of secondary and tertiary populations of intragranular precipitates, as observed on Fig. 3-c. Those precipitates are coherent with their hosting matrix grain. On the other hand and by a symmetric process, the formation of γ phase by rejection of γ-gene elements out of γ' precipitates may also occur during cooling. The mechanism by which it occurs at the rim of the γ' precipitates but inside the former envelope, leading the morphologies observed on Figs. 8-b and 8-c, remains to be clarified. However, the newly formed γ phase ends up with a shell-like shape; surrounding partially or completely all primary γ' precipitates. It is worth noting that small γ particles can also be observed inside the γ' precipitates (Fig. 8-c) and that some precipitates can be split by such particles (as shown on Fig. 8-d).

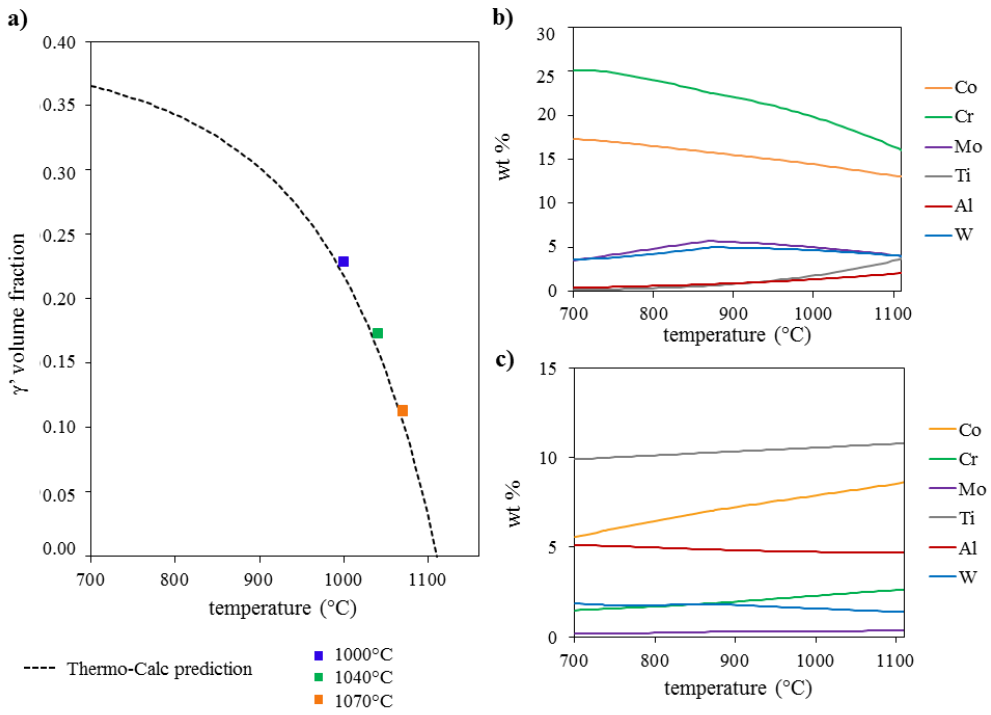

Figure 10: Thermo-Calc simulation results: a) γ' volume fraction as a function of temperature and experimentally measured fractions. b) γ and c) γ' phases composition as a function of temperature.

Once the matrix gets being deformed and stores energy, the shell starts expanding to become a HERX grain. The reason why the γ shell obviously stores less energy than the surrounding γ matrix remains to be explained. The slight difference in chemical composition between the γ shell and the γ matrix, and especially in the tungsten content, could possibly be responsible

for a different constitutive behavior of both γ phases : the γ shell, with an increased content in tungstene would be harder than the matrix and deform less. This remains to be further investigated.

The nucleation scenario based on the inverse precipitation of coherent γ phase prior to deformation explains well the location, coherency and immediate growth of a unique HERX grain per primary precipitate at low strains; as well as the uniqueness of the HERX burst in the deformed samples.

2.5. Interaction of (primary and secondary) γ' precipitates with the growing HERX grains

Figure 11 shows BSE images of partially recrystallized microstructures obtained after deformation at 1040°C or 1070°C and 0.1 s^{-1}. The recrystallized grains are only HERX grains at those low strain levels.

Some of the secondary precipitates formed during cooling after the preliminary annealing are still present in the microstructure after deformation at 1000°C or 1040°C, but they were almost completely dissolved at 1070°C. Primary and secondary γ' precipitates were quantified in samples deformed at 0.01$s^{-1}$and T = 1000°C, 1040°C, or 1070°C to ε = 0.60. At this lower strain rate, the pinning configurations are similar to those of Fig. 11 but the trends of precipitate evolutions are clearer. Precipitate sizes and volume fractions are plotted as a function of deformation temperature on Figure 12, the total γ' volume fraction is also reported on Fig. 10-a for comparison with Thermo-calc predictions. The latter reveals that the measured and predicted volume fractions are well correlated at all temperatures, with a decrease of the volume fraction as the temperature increases. The separate statistics of each population (Fig. 12-a) shows that their respective volume fractions decrease with increasing temperature. The average size (in number) of those precipitates increases slightly with increasing temperature, due to the dissolution of the smallest precipitates to the profit of larger ones.

Secondary precipitates remain after deformation at 1000°C and 1040°C in the deformed matrix grains only, not in the recrystallized grains. This suggests that they have been dissolved in the recrystallization front [41] and did not reprecipitate behind it. According to Porter and Ralph, the high solubility and diffusivity of γ'-gene elements in the recrystallization front can indeed lead to the complete dissolution of intragranular particles in the recrystallization interface, if their volume fraction is low (typically <0.08) [12].

In the partially recrystallized sample of Fig. 11-a (1040°C), the remaining secondary precipitates located inside the deformed matrix are able to pin the migrating recrystallization front, more precisely the HERX grains at this stage. A possible explanation is that the recrystallization front has become saturated in γ' elements after having dissolved some secondary precipitates.

On the other hand, at 1070°C, the HERX grains get pinned by primary γ' precipitates as visible on Fig. 11-b. Five HERX grains and their γ' precipitates are presented on Fig. 11-b. The coherency of the grains surrounding precipitates 1, 3, 4 and 5 is confirmed by the

presence of twin boundaries prolonged across the γ-γ' interface. The precipitate numbered "4" pins the boundary of the grain number "3". So does the precipitate number "5" for the boundary of the grain number "4".

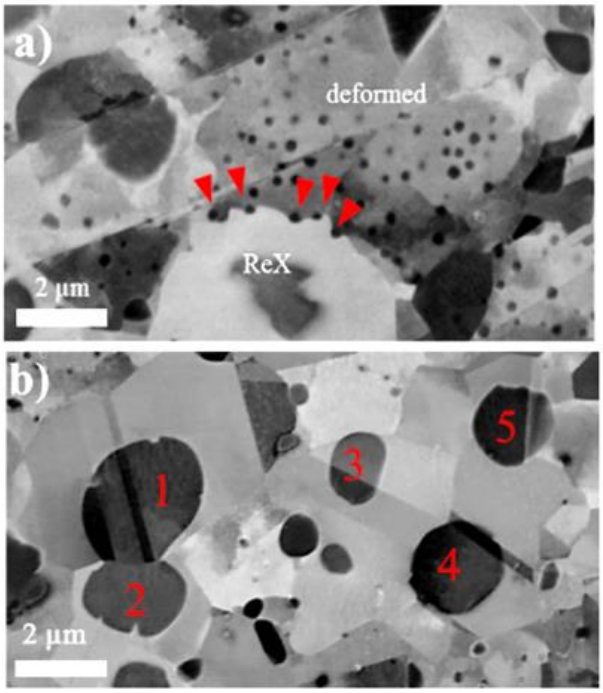

Figure 11: Heteroepitaxially recrystallized grains pinned by a) remaining secondary precipitates in the deformed matrix after deformation at T=1040°C, 0.1s^{-1} and ε=0.36, b) primary precipitates having initiated other HERX grains observed after deformation at 1070°C, 0.1s^{-1} and ε=0.3.

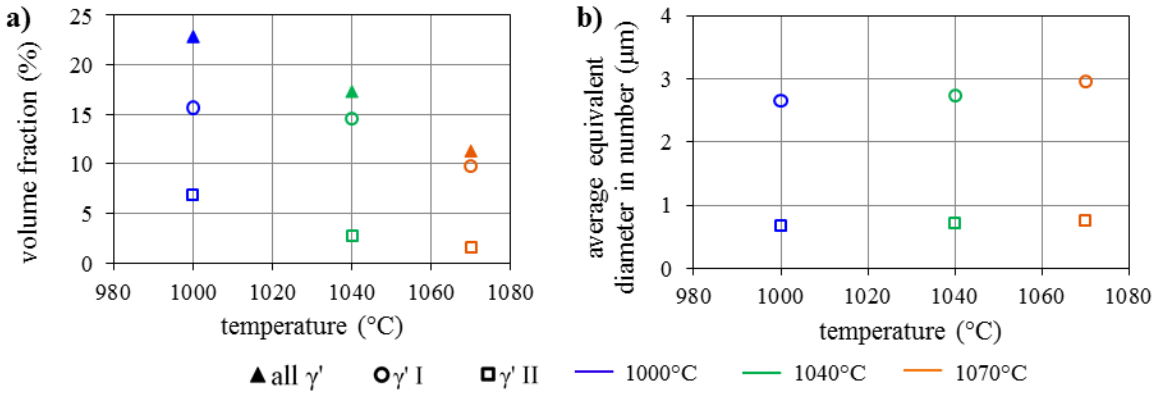

Figure 12: Evolution of primary and secondary γ' precipitate distributions in samples deformed at 0.01s^{-1}, ε=0.60 and T=1000°C, 1040°C, or 1070°C. a) γ' precipitate volume fraction, b) number-averaged equivalent circle diameter of the precipitates.

The recrystallized grain size results from the balance between the driving force associated to the difference in stored energy between neighboring grains, the capillarity force associated to the curvature radius of grain boundaries, and the Smith-Zener pinning pressure which is exerted by γ' precipitates on grain boundaries.

Using data of Fig. 12, the Smith-Zener pinning pressure exerted by the particles on moving grain boundaries was calculated using the formula (1) , established for coherent particles by Ashby et al. [42]:

$$P_{Zener,coherent} = \frac{6\gamma f_V}{d} \quad (1)$$

where γ is the grain boundary energy (0.75 J/m² for a similar nickel based alloy around 1000°C [43]), f_V is the volume fraction and d the number-average diameter of second phase particles.

Table 2: Estimation of the pinning forces associated to primary and secondary precipitates at each tested temperature.

Temperature (°C)	1000	1040	1070
P_{Zener} (γ'_I) (10^3 kPa)	2.1	1.9	1.2
P_{Zener} (γ'_{II}) (10^3 kPa)	3.7	1.4	0.4

Table 2 compares the magnitude of the pinning pressures associated with each precipitate population at all tested temperatures. At 1000°C, secondary precipitates generate the highest pinning pressure. At higher temperatures, they progressively dissolve (Fig. 12-a), which leads to a decrease in their pinning pressure. Primary precipitates become the strongest pinning population at 1070°C. This trend is fully consistent with the observations of Figure 11: the recrystallization front is pinned by secondary precipitates at low temperatures and primary ones at high temperatures.

The HERX grains developing at 1070°C interact with primary precipitates only, and reach larger sizes than those growing at lower temperatures which are submitted to a higher pinning force exerted by the secondary precipitates (5.5 versus 2.5 μm, see Fig.7c).

Conclusions

- This article demonstrates the occurrence of a new recrystallization mechanism in the commercial γ-γ' nickel based superalloy René 65™ submitted to sub-solvus deformation.
- This mechanism is initiated by inverse precipitation of γ phase occurring prior to deformation at the rim of primary γ' precipitates, as a result of their supersaturation in γ-gene elements. This transformation leads to the formation of a (complete or partial) coherent γ shell around the primary precipitates, which later on behaves as a recrystallization nucleus when the material starts being deformed. This nucleus then grows under a difference in stored energy with the surrounding γ matrix, and transforms into a recrystallized grain which remains coherent with the involved γ' precipitate. The development of such grains leads to wide multi-micrometric coherent

γ-γ’ structures which were recently reported by the authors [32] . Consistently, this mechanism was named "heteroepitaxial recrystallization" (HERX).

- The interaction of HERX with classical discontinuous dynamic recrystallization (DDRX) was studied at 1000°C, 1040°C and 1070°C. HERX always starts before DDRX. The subsequent development of DDRX grains consumes the HERX grains. The later may eventually completely disappear at high strains.
- This mechanism brings us to reconsider the role of primary γ’ precipitates in the dynamic recrystallization processes of γ-γ’ superalloys: they do not only pin the grain boundaries, controlling the final grain size, but can also truly initiate recrystallization phenomena.
- Alghouth it was presented here in the René 65 alloy, this mechanism may occur in other γ-γ’ superalloys exhibiting a low lattice mismatch and a suitable thermochemical behavior.

Acknowledgements :

The authors are grateful to Pr. J.-M. Fiorani from Institut Jean Lamour (Nancy, France) who ran the Thermo-Calc calculations.

Bibliography

[1] R.C. Reed, The Superalloys, Cambridge University Press, Cambridge, 2006. doi:10.1017/CBO9780511541285.

[2] G. Shen, S.L. Semiatin, R. Shivpuri, Modeling microstructural development during the forging of Waspaloy, Metall. Mater. Trans. A. 26 (1995) 1795–1803. doi:10.1007/BF02670767.

[3] S.. Medeiros, Y.V.R.. Prasad, W.. Frazier, R. Srinivasan, Microstructural modeling of metadynamic recrystallization in hot working of IN 718 superalloy, Mater. Sci. Eng. A. 293 (2000) 198–207. doi:10.1016/S0921-5093(00)01053-4.

[4] Q. Guo, D. Li, S. Guo, H. Peng, J. Hu, The effect of deformation temperature on the microstructure evolution of Inconel 625 superalloy, J. Nucl. Mater. 414 (2011) 440–450. doi:10.1016/j.jnucmat.2011.05.029.

[5] S. Mitsche, C. Sommitsch, D. Huber, M. Stockinger, P. Poelt, Assessment of dynamic softening mechanisms in Allvac® 718Plus™ by EBSD analysis, Mater. Sci. Eng. A. 528 (2011) 3754–3760. doi:10.1016/j.msea.2011.01.044.

[6] B. Lindsley, X. Pierron, Sub-solvus recrystallization mechanisms in UDIMET (R) alloy 720LI, SUPERALLOYS 2000. (2000) 59–68.

[7] H. Zhang, K. Zhang, S. Jiang, H. Zhou, C. Zhao, X. Yang, Dynamic recrystallization behavior of a γ′-hardened nickel-based superalloy during hot deformation, J. Alloys Compd. 623 (2015) 374–385. doi:10.1016/j.jallcom.2014.11.056.

[8] Y.C. Lin, X.-Y. Wu, X.-M. Chen, J. Chen, D.-X. Wen, J.-L. Zhang, et al., EBSD study of a hot deformed nickel-based superalloy, J. Alloys Compd. 640 (2015) 101–113. doi:10.1016/j.jallcom.2015.04.008.

[9] B.J. Bond, C.M. O'Brien, J.L. Russell, J.A. Heaney, M.L. Lasonde, René 65 Billet Material for Forged Turbine Components, in: U. John Wiley & sons, Inc., Hoboken, NJ (Ed.), 8th Int. Symp. Superalloys718 Deriv., 2014: pp. 107–118. doi:10.1002/9781119016854.ch9.

[10] A.J. Porter, B. Ralph, Recrystallization of a nickel-base superalloy: Kinetics and microstructural development, Mater. Sci. Eng. 59 (1983) 69–78. doi:10.1016/0025-5416(83)90089-7.

[11] J. BEE, A. JONES, P. HOWELL, The interaction of recrystallizing interfaces with intragranular precipitate dispersions in a Nickel-base super-alloy, J. Mater. Sci. 16 (1981) 1471–1476.

[12] A. Porter, B. Ralph, The recrystallization of nickel-base superalloys, J. Mater. Sci. 16 (1981) 707–713. doi:10.1007/BF00552209.

[13] R.J. Mitchell, M. Preuss, M.C. Hardy, The influence of cooling rate from temperatures above the γ′ solvus on morphology, mismatch and hardness in advanced polycrystalline nickel-base superalloys, Mater. Sci. Eng. A. 473 (2008) 158–165. doi:10.1016/j.msea.2007.04.098.

[14] J. Tiley, G.B. Viswanathan, R. Srinivasan, R. Banerjee, D.M. Dimiduk, H.L. Fraser, Coarsening kinetics of γ′ precipitates in the commercial nickel base Superalloy René 88 DT, Acta Mater. 57 (2009) 2538–2549. doi:10.1016/j.actamat.2009.02.010.

[15] A.R.P. Singh, S. Nag, S. Chattopadhyay, Y. Ren, J. Tiley, G.B. Viswanathan, et al., Mechanisms related to different generations of γ′ precipitation during continuous cooling of a nickel base superalloy, Acta Mater. 61 (2013) 280–293. doi:10.1016/j.actamat.2012.09.058.

[16] A.R.P. Singh, S. Nag, J.Y. Hwang, G.B. Viswanathan, J. Tiley, R. Srinivasan, et al., Influence of cooling rate on the development of multiple generations of γ′ precipitates in a commercial nickel base superalloy, Mater. Charact. 62 (2011) 878–886. doi:10.1016/j.matchar.2011.06.002.

[17] M. Fahrmann, A. Suzuki, Effect of cooling rate on Gleeble hot ductility of UDIMET alloy 720 billet, SUPERALLOYS 2008. (2008) 311–316.

[18] R.A. Ricks, A.J. Porter, R.C. Ecob, The growth of γ′ precipitates in nickel-base superalloys, Acta Metall. 31 (1983) 43–53. doi:10.1016/0001-6160(83)90062-7.

[19] M. Durand-Charre, The Microstructure of Superalloys, Gordon and Breach Science Publishers, 1998.

[20] K. Song, M. Aindow, Grain growth and particle pinning in a model Ni-based superalloy, Mater. Sci. Eng. A. 479 (2008) 365–372. doi:10.1016/j.msea.2007.09.055.

[21] L. Wang, G. Xie, J. Zhang, L.H. Lou, On the role of carbides during the recrystallization of a directionally solidified nickel-base superalloy, Scr. Mater. 55 (2006) 457–460. doi:10.1016/j.scriptamat.2006.05.013.

[22] L.P. Troeger, E.A. Starke, Particle-stimulated nucleation of recrystallization for grain-size control and superplasticity in an Al–Mg–Si–Cu alloy, Mater. Sci. Eng. A. 293 (2000) 19–29. doi:10.1016/S0921-5093(00)01235-1.

[23] W. XU, M. FERRY, J. CAIRNEY, F. HUMPHREYS, Three-dimensional investigation of particle-stimulated nucleation in a nickel alloy, Acta Mater. 55 (2007) 5157–5167. doi:10.1016/j.actamat.2007.05.045.

[24] L.P. Troeger, E.A. Starke, Particle-stimulated nucleation of recrystallization for grain-size control and superplasticity in an Al–Mg–Si–Cu alloy, Mater. Sci. Eng. A. 293 (2000) 19–29. doi:10.1016/S0921-5093(00)01235-1.

[25] J.D. Robson, D.T. Henry, B. Davis, Particle effects on recrystallization in magnesium–manganese alloys: Particle-stimulated nucleation, Acta Mater. 57 (2009) 2739–2747. doi:10.1016/j.actamat.2009.02.032.

[26] O. Daaland, E. Nes, Recrystallization texture development in commercial Al□Mn□Mg alloys, Acta Mater. 44 (1996) 1413–1435. doi:10.1016/1359-6454(95)00290-1.

[27] F.. Humphreys, Particle stimulated nucleation of recrystallization at silica particles in nickel, Scr. Mater. 43 (2000) 591–596. doi:10.1016/S1359-6462(00)00442-5.

[28] J.D. Robson, Microstructural evolution in aluminium alloy 7050 during processing, Mater. Sci. Eng. A. 382 (2004) 112–121. doi:10.1016/j.msea.2004.05.006.

[29] F.J. Humphreys, A unified theory of recovery, recrystallization and grain growth, based on the stability and growth of cellular microstructures—II. The effect of second-phase particles, Acta Mater. 45 (1997) 5031–5039. doi:10.1016/S1359-6454(97)00173-0.

[30] S.L. Semiatin, D.S. Weaver, R.C. Kramb, P.N. Fagin, M.G. Glavicic, R.L. Goetz, et al., Deformation and recrystallization behavior during hot working of a coarse-grain, nickel-base superalloy ingot material, Metall. Mater. Trans. A. 35 (2004) 679–693. doi:10.1007/s11661-004-0379-y.

[31] C.M. Heaney, M.L. Lasonde, A.M. Powell, B.J. Bond, C.M. O'Brien, Development of a New Cast and Wrought Alloy (René 65) for High Temperature Disk Applications, in: U. John Wiley & Sons (Ed.), 8th Int. Symp. Superalloy 718 Deriv., 2014: pp. 67–77.

[32] M.-A. Charpagne, P. Vennéguès, T. Billot, J.-M. Franchet, N. Bozzolo, Evidence of multimicrometric coherent γ' precipitates in a γ-γ' Nickel-based superalloy, J. Microsc. (2016). http://onlinelibrary.wiley.com/doi/10.1111/jmi.12380/full.

[33] J. RADAVICH, W. COUTS, Effect of temperature exposure on the microstructure of 4.5 Al-3.5 Ti Nickel-base alloy, Trans. ASM. 54 (1961) 591–597.

[34] J. RADAVICH, W. COUTS, Metallography of the superalloys, Rev. High Temp. Mater. 1 (1971) 55–96.

[35] H.F. Merrick, Precipitation within γ' particles in nickel-base superalloys, Metall. Trans. 4 (1973) 885–887. doi:10.1007/BF02643103.

[36] M.. Miller, R. Jayaram, L.. Lin, A.. Cetel, APFIM characterization of single-crystal PWA 1480 nickel-base superalloy, Appl. Surf. Sci. 76-77 (1994) 172–176. doi:10.1016/0169-4332(94)90339-5.

[37] E. Cadel, D. Lemarchand, S. Chambreland, D. Blavette, Atom probe tomography investigation of the microstructure of superalloys N18, Acta Mater. 50 (2002) 957–966. doi:10.1016/S1359-6454(01)00395-0.

[38] Y. Yuan, Y.F. Gu, Z.H. Zhong, Z. Shi, T. Osada, T. Yokokawa, et al., γ precipitation in the primary γ′ of a new Ni–Co-base disc superalloy, Mater. Sci. Eng. A. 579 (2013) 35–40. doi:10.1016/j.msea.2013.05.011.

[39] B. Flageolet, M. Jouiad, P. Villechaise, J. Mendez, On the role of γ particles within γ′ precipitates on damage accumulation in the P/M nickel-base superalloy N18, Mater. Sci. Eng. A. 399 (2005) 199–205. doi:10.1016/j.msea.2005.04.006.

[40] J.M. Oblak, J.E. Doherty, A.F. Giamei, B.H. Kear, Precipitation of γ in the γ′ of nickel-base superalloys, Metall. Trans. 5 (1974) 1252–1255. doi:10.1007/BF02644342.

[41] K. Smidoda, W. Gottschalk, H. Gleiter, Diffusion in migrating interfaces, Acta Metall. 26 (1978) 1833–1836. doi:10.1016/0001-6160(78)90095-0.

[42] M. ASHBY, J. HARPER, J. LEWIS, INTERACTION OF CRYSTAL BOUNDARIES WITH SECOND-PHASE PARTICLES, Trans. Metall. Soc. AIME. 245 (1969) 413–&.

[43] L. E. Murr, Interfacial Phenomena in Metals and Alloys, 1975.